ELSEVIER

Materials Science and Engineering A249 (1998) 22–29

MATERIALS SCIENCE & ENGINEERING A

Experimental observation and computational simulation of dynamic void collapse in single crystal cooper

Sia Nemat-Nasser *, Tomoo Okinaka [1], Vitali Nesterenko

Center of Excellence for Advanced Materials, Department of Applied Mechanics and Engineering Sciences, University of California at San Diego, 9500 Gilman Drive, La Jolla, San Diego CA, 92093-0416, USA

Abstract

Hollow circular cylinders of single crystal copper are subjected to externally applied explosive loads that cause the collapse of the cylinder. Then numerical simulations are performed to understand the deformation process that leads to localized deformation and tensile cracking, observed in partially collapsed cylinders of fcc single crystals. The results of experiments and numerical simulations are in good agreement.

Keywords: Computational simulations; Dynamic void collapse; Single crystal copper

1. Introduction

The objective of this research is to study the localization of the inelastic flow and the possible subsequent crack propagation in single crystals by experiment and by numerical simulations; focusing on the anisotropic inelastic response and mechanisms of possible crack initiation and growth, produced upon unloading by the residual inhomogeneous plastic strains. A detailed study of such inelastic flow localization and crack propagation is important, since strain localization in single crystals can lead to global instability.

In a recent paper, an experimental technique, called the 'thick-walled cylinder (TWC) method', has been used by Nesterenko et al. [1] and Bondar and Nesterenko [2] to study strain localization at high strain rates. The strain rate in the TWC method can be much higher than the strain rate that can be achieved by conventional methods, such as the Hopkinson bar technique. Nesterenko and Bondar [3] observed shear-banding and cracking under high strain rate conditions in various polycrystalline materials, such as copper, stainless steel, aluminum and niobium.

The dynamic void collapse and void growth in single crystals under uniform far-field stresses were studied analytically by Nemat-Nasser and Hori [4], showing that tension cracks can be produced upon unloading in a direction normal to the applied compression. Nemat-Nasser and Chang [5] followed this analytical work and experimentally illustrated the basic phenomenon using the Hopkinson bar technique. They observed that cracks propagate into the recrystallized grains at the nominal strain rate of $\approx 10^4\ s^{-1}$, which corresponds to local strain rates exceeding $10^6\ s^{-1}$, near the boundaries of a collapsing void. Nemat-Nasser and Chang discuss the mechanism of the formation of Lomer–Cottrell sessile dislocations during loading, which can then lead to fracturing during unloading. Their SEM microscopy seems to support this explanation. Cuitino and Ortiz [6] seek to explore the possibility of vacancy condensation as a void-nucleating mechanism in fcc single crystals at large plastic deformations, and suggest that high strain rates inhibit void-nucleation and promote brittle fracture in the experiments of Nemat-Nasser and Chang [5]. An earlier analysis of Nemat-Nasser and Hori [4] showed development of high tensile stresses at the tips of a collapsed void, once the applied compression is removed.

Here, we study the localization of inelastic flow and the subsequent crack propagation in fcc single crystals under uniform high strain rate compressive loading, using the TWC method. Then, numerical simulations,

* Corresponding author. Tel.: +1 619 5344914; fax: +1 619 5342727; e-mail: sia@halebopp.ucsd.edu

[1] Current address: Department of Civil Engineering, Kinki University.

0921-5093/98/$19.00
PII S0921-5093(98)00559-0

are performed to explore the details of this process. A new algorithm to simulate finite deformation of fcc single crystals, proposed by Nemat-Nasser and Okinaka [7] is implemented into the finite-deformation code, DYNA2D, and used for the simulation. Our results support the conclusion of Nemat-Nasser and Hori [4], that tensile cracking is caused by unloading in the presence of inhomogeneous plastic strains.

2. Experimental procedure and results

Externally applied explosives are used to collapse a thick-walled cylinder of single crystal copper. The specimen consists of a hollow cylindrical tube of single crystal copper encased in a polycrystal copper jacket. The single crystal tube is cut from a single crystal rod, using a spark erosion technique. Then the sample is loaded by detonating an explosive which surrounds the specimen cell. The magnitude of the explosive is carefully chosen to ensure either full or partial collapse of the hollow cylindrical specimen. The size and shape of the hollow cylindrical specimen, and the overall experimental set-up for the TWC method are shown in Figs. 1 and 2, respectively. The initial configuration of the single crystal is measured from the remaining part of the sample using X-ray diffraction. The axis of the cylinder is found to be in the [1 3 4]-direction.

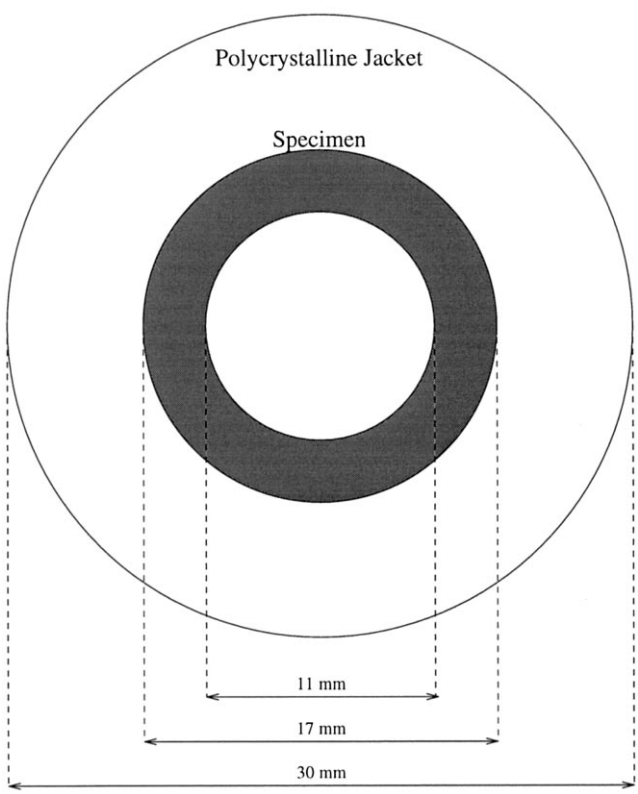

Fig. 1. Shape and size of the specimen used in the experiment.

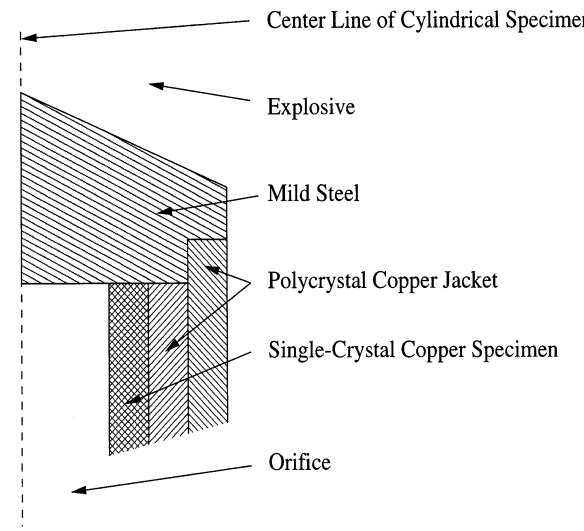

Fig. 2. Experimental set-up, showing half of the cross-section through the center line of the cylindrical specimen.

In the first experiment, the hollow cylindrical single-crystal specimen is fully collapsed under conditions that have been discussed by Nesterenko and Bondar [3]. The detonation speed measured in this particular experiment was $\mathscr{D} = 4030\ \mathrm{m\,s^{-1}}$ (explosive-ammonite plus sand (10 vol.%) with a density $1\ \mathrm{g\,cm^{-3}}$), with the diameter of the explosive charge being 60 mm. The detonation pressure is estimated using

$$P = \frac{\rho \mathscr{D}^2}{\kappa + 1}, \quad \kappa \approx 3, \tag{2.1}$$

which gives 4 GPa. The initial radial velocity of the inner boundary of the specimen is measured by the non-contact electromagnetic method and is $\approx 200\ \mathrm{m\,s^{-1}}$, leading to the time of collapse of $\approx 8\ \mu\mathrm{s}$.

Optical micrographs of the overall and the central region of the collapsed specimen are shown in Figs. 3

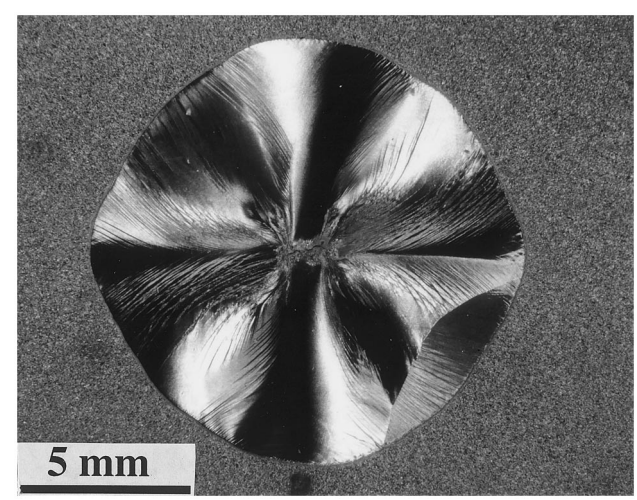

Fig. 3. Optical micrograph of the fully collapsed specimen.

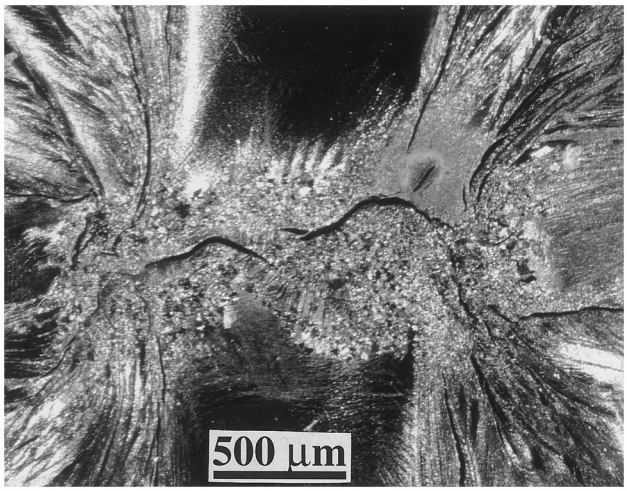

Fig. 4. Optical micrograph of the central part of the fully collapsed specimen. The central curved crack is the folded inner boundary of the collapsed cylinder. Lines around the central curve are flow localization zones.

and 4, respectively. Fig. 3 shows that the outer boundary of the collapsed specimen is non-circular. The lines of the shear-banding, running from the outer boundary to the collapsed inner boundary, are also seen in this figure. In Fig. 4, the central curved lines are the folded inner boundary of the cylinder. Lines of the flow localization are also observed around the central folds in this picture. Since the shape of the outer part of the jacket of the specimen and the loading condition are axially symmetric, it can be concluded that the localization is caused by the anisotropic inelastic response of the single crystal.

Next, the loading condition is estimated for a partially collapsed specimen, and is used to simulate the crack initiation and propagation which occur upon unloading. To ensure an incomplete void collapse, a suitably smaller explosive loading was chosen. The outer diameter of the explosive charge was decreased to 55 mm, resulting in a smaller detonation speed $\mathscr{D} \approx 3030\ \mathrm{m\,s^{-1}}$. According to Eq. (2.1), this gives a detonation pressure of ≈ 2.3 GPa, leading to an incomplete collapse.

The central part of the specimen is shown in Fig. 5. The outer boundary of single crystal develops a non-circular shape. The inner boundary, which has a circular shape initially, develops a rectangular shape, and cracks are initiated at four corners of the rectangle. Shear-bands develop around the four cracks, and also, from the outer boundary to the upper and bottom segments of the inner boundary of the cylinder. However, the mechanism of crack initiation and propagation is not revealed by these observations. Hence, numerical simulations are used to examine this process and to develop a detailed understanding of the phenomemon.

3. Numerical simulations

3.1. Kinematics and constitutive relations

In this subsection, first the fundamentals of the general kinematics, on which the numerical calculation is based, are briefly reviewed. The general kinematics of the elastic–plastic deformation of crystals at finite strains are given by Hill [8], Rice [9], Hill and Rice [10] and others. Reviews are given by Nemat-Nasser [11], Asaro [12] and Havner [13].

The total deformation gradient, $\boldsymbol{F}$, is divided into a *non-plastic* (elastic plus rigid-body rotation) deformation gradient, $\boldsymbol{F}^*$, and a *plastic* deformation gradient, $\boldsymbol{F}^{\mathrm{p}}$, as follows:

$$\boldsymbol{F} = \boldsymbol{F}^*\boldsymbol{F}^{\mathrm{p}}. \tag{3.1}$$

The velocity gradient is defined by

$$\boldsymbol{L} = \dot{\boldsymbol{F}}\boldsymbol{F}^{-1}, \tag{3.2a}$$

where the dot stands for the time derivative. Similarly, the non-plastic velocity gradient, $\boldsymbol{L}^*$, and the plastic velocity gradient, $\boldsymbol{L}^{\mathrm{p}}$, are given by

$$\boldsymbol{L}^* = \dot{\boldsymbol{F}}^*\boldsymbol{F}^{*-1}, \tag{3.2b}$$

and

$$\hat{\boldsymbol{L}}^{\mathrm{p}} = \dot{\boldsymbol{F}}^*\boldsymbol{F}^{\mathrm{p}-1}, \tag{3.2c}$$

where the hat is used to denote that the velocity gradient is measured with respect to the *initial configuration* of the crystal lattice. Substitution of Eq. (3.1) and Eqs. (3.2b) and (3.2c) into Eq. (3.2a) yields

$$\boldsymbol{L} = \boldsymbol{L}^* + \boldsymbol{F}^*\hat{\boldsymbol{L}}^{\mathrm{p}}\boldsymbol{F}^{*-1}. \tag{3.2d}$$

It is assumed in this work that the plastic deformation is solely due to the crystalline slip. Hence, the plastic velocity gradient, $\hat{\boldsymbol{L}}^{\mathrm{p}}$ is given by the sum of the

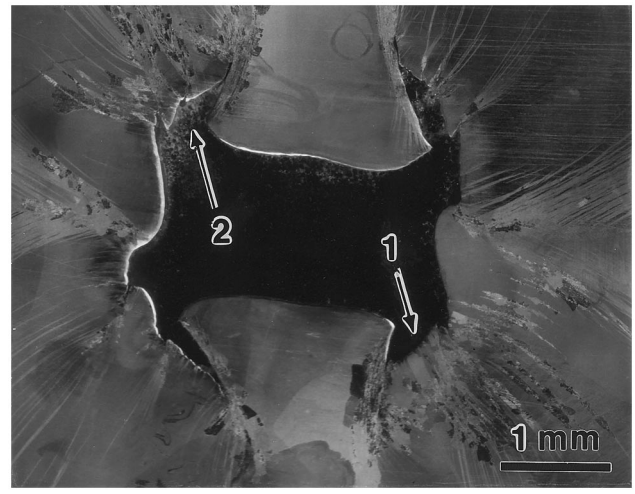

Fig. 5. Optical micrograph of the partially collapsed specimen, central part.

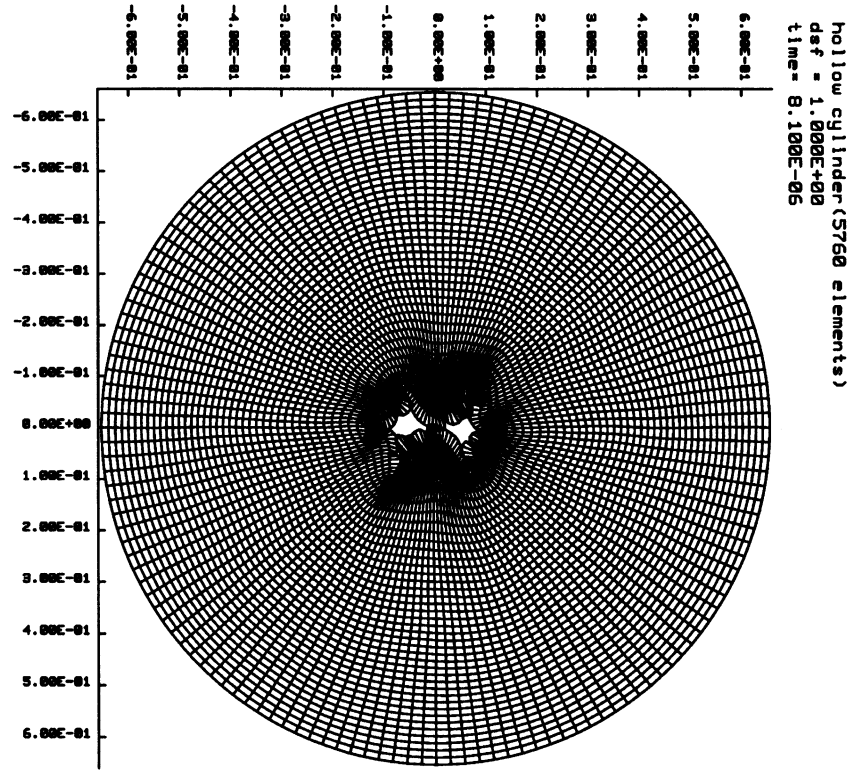

(a)

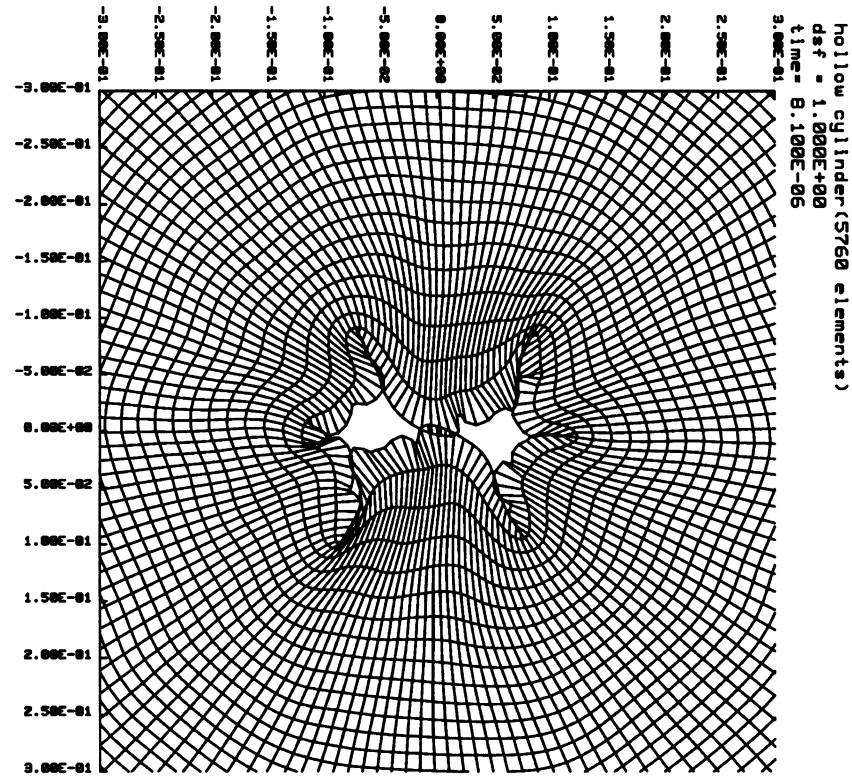

(b)

Fig. 6. Final deformation state of the fully collapsed specimen at 8.1 μs: (a) overall configuration, and (b) central part.

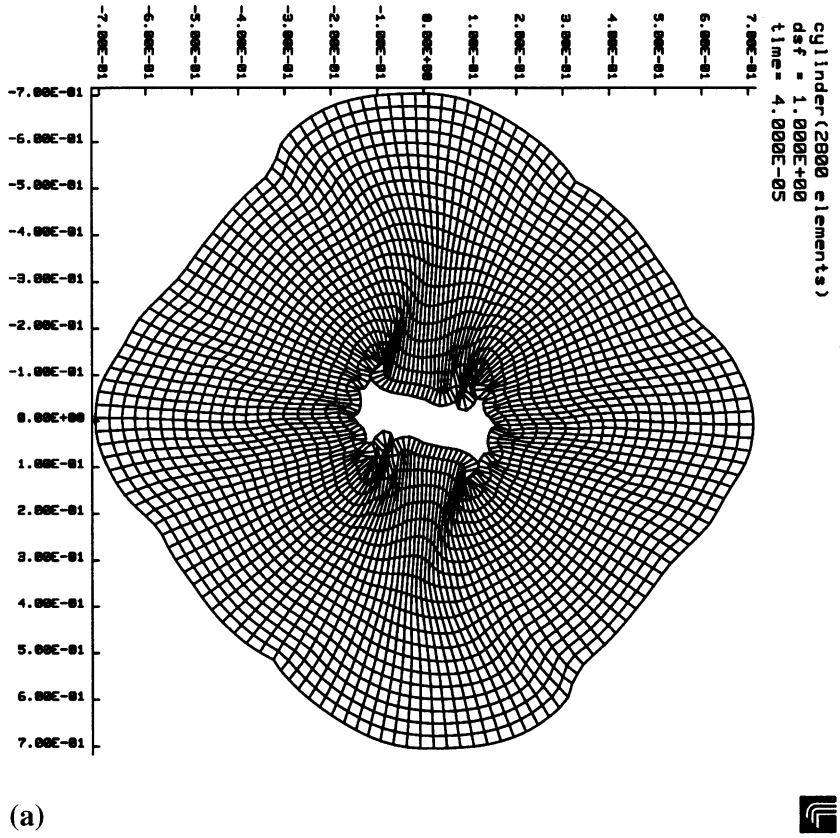

(a)

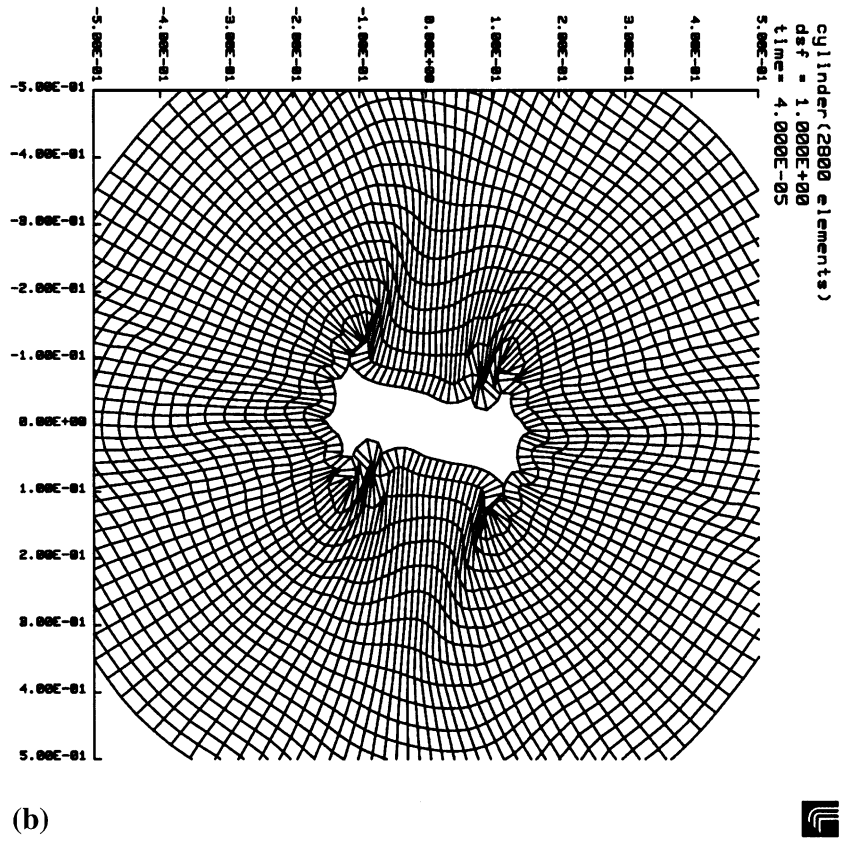

(b)

Fig. 7. Final deformation state of the (134)-cylinder at 40.0 μs: (a) overall configuration, and (b) central part. Loading is removed at 1.1 μs in this simulation.

slips of all slip systems. Since the fcc single crystals have four slip planes and three slip directions on each plane, it follows that

$$\hat{\boldsymbol{L}}^{\mathrm{p}} = \sum_{\alpha=1}^{4} \sum_{a=1}^{3} \dot{\gamma}^{(\alpha a)} \boldsymbol{l}_0^{(\alpha a)}, \tag{3.3}$$

where $\dot{\gamma}^{(\alpha a)}$ is a slip rate, and $\boldsymbol{l}_0^{(\alpha a)}$ is the ath slip direction on the αth slip plane, which is defined by

$$\boldsymbol{l}_0^{(\alpha a)} = \boldsymbol{s}_0^{(\alpha a)} \otimes \boldsymbol{n}_0^{(\alpha)}. \tag{3.4}$$

Here, $\boldsymbol{s}^{(\alpha a)}$ and $\boldsymbol{n}^{(\alpha)}$ are the slip direction and the slip plane normal, respectively, and the subscript 0 stands for the initial configuration of the lattice. From Eqs. (3.2d) and (3.3), we obtain

$$\boldsymbol{L} = \boldsymbol{L}^* + \sum_{\alpha=1}^{4} \sum_{a=1}^{3} \dot{\gamma}^{(\alpha a)} \boldsymbol{l}^{(\alpha a)}. \tag{3.5a}$$

Since the elastic strains are generally small, it is reasonable to neglect them in comparison with the lattice rotation. Hence, set

$$\boldsymbol{l}^{(\alpha a)} = \boldsymbol{R}^* \boldsymbol{l}_0^{(\alpha a)} \boldsymbol{R}^{*T}, \tag{3.6}$$

where $\boldsymbol{R}^*$ is the lattice rotation tensor. With small elastic strains, the non-plastic velocity gradient becomes

$$\boldsymbol{L}^* = \dot{\varepsilon} + \varepsilon \boldsymbol{\Omega}^* - \boldsymbol{\Omega}^* \varepsilon + \boldsymbol{\Omega}^*, \tag{3.7}$$

where ε is the lattice elastic strain, measured in the rotated lattice, and $\boldsymbol{\Omega}^*$ is the lattice spin rate defined by

$$\boldsymbol{\Omega}^* = \dot{\boldsymbol{R}}^* \boldsymbol{R}^{*T}. \tag{3.8}$$

The symmetric and antisymmetric parts of Eq. (3.5a) are given by

$$\boldsymbol{D} = \boldsymbol{D}^* + \sum_{\alpha=1}^{4} \sum_{a=1}^{3} \dot{\gamma}^{(\alpha a)} \boldsymbol{p}^{(\alpha a)}, \tag{3.5b}$$

and

$$\boldsymbol{W} = \boldsymbol{W}^* + \sum_{\alpha=1}^{4} \sum_{a=1}^{3} \dot{\gamma}^{(\alpha a)} \boldsymbol{w}^{(\alpha a)}, \tag{3.5c}$$

where $\boldsymbol{D}^*$ and $\boldsymbol{W}^*$ are the symmetric and antisymmetric parts of the non-plastic velocity gradient, $\boldsymbol{L}^*$, respectively. Also, $\boldsymbol{p}^{(\alpha a)}$ and $\boldsymbol{w}^{(\alpha a)}$ are the symmetric and antisymmetric parts of the slip system tensor, $\boldsymbol{l}^{(\alpha a)}$, respectively.

Linear elasticity is used to model the elastic lattice distortion,

$$\overset{\nabla}{\boldsymbol{\sigma}} = \boldsymbol{C}^* : \boldsymbol{D}^*, \tag{3.9}$$

where $\overset{\nabla}{\boldsymbol{\sigma}}$ and $\boldsymbol{C}^*$ are the Jaumann rate of the Cauchy stress and the elasticity tensor in the rotated lattice, respectively.

The rate-dependent slip model with the power law is employed to model the crystalline slip. Hence, the slip rate of the (αa)th slip system is assumed to be given by

$$\dot{\gamma}^{(\alpha a)} = \dot{\gamma}_0^{(\alpha a)} \operatorname{sgn}(\tau^{(\alpha a)}) \left| \frac{\tau^{(\alpha a)}}{\tau_Y^{(\alpha a)}} \right|^m, \tag{3.10}$$

where $\tau^{(\alpha a)} = \langle \boldsymbol{\sigma}, \boldsymbol{p}^{(\alpha a)} \rangle$ is the resolved shear stress, and

$$\operatorname{sgn}(x) = \begin{cases} 1 & \text{for } x \geq 0 \\ -1 & \text{for } x < 0. \end{cases} \tag{3.11}$$

In equation Eq. (3.10), $\tau_Y^{(\alpha a)}$ and $\dot{\gamma}_0^{(\alpha a)}$ are the critical resolved shear stress and the reference value of the slip rate, respectively. A linear strain-hardening model is considered. The critical resolved shear stress, $\tau_Y^{(\alpha a)}$, is thus expressed as

$$\tau_Y^{(\alpha a)} = \sum_{\beta=1}^{4} \sum_{b=1}^{3} h(\gamma)_{(\beta b)}^{(\alpha a)} \gamma^{(\beta b)}, \tag{3.12a}$$

where

$$\gamma = \sum_{\alpha=1}^{4} \sum_{a=1}^{3} \int \left| \dot{\gamma}^{(\alpha a)} \right| \mathrm{d}\xi. \tag{3.12b}$$

While thermal softening can be included in the power law model, as in Nemat-Nasser et al. [14], this effect is neglected in the present case, since the flow stress of copper is relatively small and it's heat conductivity is rather high.

An efficient algorithm to solve Eq. (3.5b) incrementally for a given constant $\boldsymbol{D}$ has been proposed by Nemat-Nasser and Okinaka [7]. In the present work, this new algorithm is implemented into the finite deformation code DYNA2D, and is used to simulate the cylinder collapse experiments numerically.

4. Numerical simulation of the fully collapsed cylinder

The initial configuration of the lattice in this simulation is chosen to correspond to the experiment, i.e. the (1 3 4)-plane. The x- and y-axes are arbitrarily chosen to coincide with the $[25\,\bar{3}\,\bar{4}]$-, and $[0\,4\,\bar{3}]$-directions in terms of the Miller indices. In the numerical simulation, the inner boundary is defined as a contact surface without friction.

The loading condition is defined in terms of the velocity of the nodes on the outer boundary of the single-crystal cylinder. Hence, nodes on the outer boundary move towards the center of the specimen with the prescribed velocity, maintaining a circular shape for this boundary. The time-variation of the radial velocity, $v_{\mathrm{r}}(t)$, is approximated by

$$v_{\mathrm{r}}(t) = A_0 \, \mathrm{e}^{-\alpha(t-t_0)^2}. \tag{4.1}$$

Next, the material property used in the simulation is discussed. Although the single-crystal copper is *elastically* anisotropic, its effect for large plastic strains and rotations is insignificant relative to that of the inelastic anisotropy, and hence, elastically isotropic material is assumed. The shear modulus and Poisson's ratio are $\mu = 45$ GPa, and $\nu = 0.33$, respectively. The rate sensi-

tivity power in Eq. (3.10) is set at $m = 101$. The initial value of the critical resolved shear stress is assumed to be 0.25% of the elastic shear modulus, so that $\tau_{Y_0} =$ 112.5 MPa. For the strain hardening, the rate of change of the critical resolved shear stress is

$$\dot{\tau}^{(\alpha a)} = \sum_{\beta=1}^{4} \sum_{b=1}^{3} h_{(\beta b)}^{(\alpha a)} \left|\dot{\gamma}^{(\beta b)}\right|. \tag{4.2}$$

Here,

$$h_{(\beta b)}^{(\alpha a)} = h(\gamma)(\delta_{(\beta b)}^{(\alpha a)} + r(1 - \delta_{(\beta b)}^{(\alpha a)})), \tag{4.3}$$

where

$$h(\gamma) = \begin{cases} 0.003125\mu & \gamma \leq 0.32 \\ \dfrac{0.003125\mu}{1.0 + 3.7(\gamma - 0.32)} & \gamma > 0.32, \end{cases} \tag{4.4}$$

$$\gamma = \sum_{\alpha=1}^{4} \sum_{a=1}^{3} \int \left|\dot{\gamma}^{(\alpha a)}\right| \mathrm{d}\xi, \tag{4.5}$$

and $r = 1.25$ is used; see Rashid and Nemat-Nasser [15]. This assumes that the latent hardening exceeds self-hardening by 25%. With this strain hardening, the critical resolved shear stress levels off at three times its initial value, after a 200% equivalent strain.

In the first simulation, the cylinder is fully collapsed at 8.1 μs. The overview and the magnified central part of the deformed mesh are shown in Fig. 6. In Fig. 6(a), the outer boundary of the collapsed specimen has a circular shape. As will be shown for the partially collapsed case, this is due to the plastic flow which continues after a complete collapse. The central part of the collapsed mesh in Fig. 6(b) is shown for comparison with the results of the experiment, Fig. 4. These two figures show good agreement, and hence, it is concluded that the central curve in the experiment is the collapsed and folded inner boundary of the cylinder and not cracks originating from the center. The lines of the flow localization are also observed around the central part of the collapsed cylinder.

In order to study the process of flow localization, the deformation states at 6.75, 7.25 and 7.75 μs were calculated. The flow localization initiates at ≈ 6.74 μs, when the initially circular inner boundary develops localization at four corners. The inner boundary then develops two parallel straight and two semicircular edges. It is observed that, among the four segments, two shrink much faster after initiation of the localization. Although the loading on the outer boundary is uniform, the anisotropic inelastic response of the single crystal leads to a non-uniform shrinking speed of the inner boundary, and hence, localization at the junction of the resulting segments.

In numerical simulations, it is clearly observed that, upon unloading, large tensile stresses develop within the localized regions. These stresses are sufficient to cause crack initiation at the inner surface of the collapsed cylinder. This observation supports earlier results of Nemat-Nasser and Hori [4].

5. Numerical simulation of the partially collapsed cylinder

Partially collapsed cylinders (Fig. 5) offer unique features whose study requires special consideration. Crack initiation on unloading in single crystals under uniform compression, is one such feature that is examined in this subsection. The initial configuration of the lattice in computer calculations coincides with the experimental sample, the cross-sectional area being the (1 3 4)-plane. Again, the x- and y-axes are arbitrarily chosen, so that they coincide with the[25 $\bar{3}$ $\bar{4}$]-, and [0 4 $\bar{3}$]-directions, respectively. Nodes on the outer boundary are moved toward the center of the specimen with the given velocity, according to Eq. (4.1), until 1.1 μs. The given loading condition is then removed, rendering the outer boundary traction-free. This leads to an incomplete collapse of the cylinder.

The central part of the deformed mesh at 40 μs, are shown in Fig. 7(b). Fig. 7(b) shows excellent correlation with the results of the experiment, shown in Fig. 5. It is noteworthy that the similarity between the simulation and the experiment is observed not only in the flow localization around the inner boundary, but also in the shape of the outer boundary after unloading. The non-circular shape of the outer boundary of the unloaded specimen, shown in Fig. 3, has been one of our main concerns, since it might have been caused by the variation of the explosive loading, through a uniform loading may be expected. However, comparison with simulation reveals that this geometry is caused by the anisotropic inelastic response of the single crystal.

6. Conclusion

Localization of inelastic flow in fcc single crystals is studied experimentally and by numerical simulations. The TWC method is used in the experiment. Numerical simulations are performed to examine the deformation process which leads to the observed final configuration. The new algorithm, proposed by Nemat-Nasser and Okinaka [7], is implemented into the finite deformation code, DYNA2D, in order to perform these simulations. Various initial configurations of the lattice are examined in the numerical simulation to study their effect on the flow localization phenomena.

The flow localization in fcc single crystals due to their anisotropy inelastic response is observed experimentally. The process of the localization is studied in detail through numerical simulations, and the comparison of the results with those of experiments shows remarkable agreements.

Crack initiation and propagation in fcc single crystals are observed in experiments, and crack initiation is successfully simulated by numerical calculations. Through the numerical simulation, it is concluded that cracks are produced during the unloading process by the tensile stresses which are produced by large heterogeneous plastic deformations that occur during the loading regime, which supports a similar result reported earlier by Nemat-Nasser and Hori [4].

Acknowledgements

This research was supported by the Army Research Office under contract number ARO DAAL 03-92-G-0108, and the National Science Foundation under contract number MSS-90-21671 to the University of California, San Diego. Support for V.F. Nesterenko was provided by ONR, grant N00014-94-1-1040, Program Officer Dr J. Goldwasser. The authors wish to thank ARO and NSF for their support and to Dr Bondar and Y. Lukyanov for help with experiments, Dr M. Liu for help in microscopy, and Professor M.A. Meyers for providing monocrystal specimens. Thanks are also due to Dr M. Beizai who helped with the preparation of the manuscript. The computations reported here are carried out on the CRAY–C90 at the San Diego Supercomputer Center, access to which was made possible by the National Science Foundation.

References

[1] V.F. Nesterenko, A. Lazaridi, S. Pershin, Fiz. Goren. Vzryva. 25 (1989) 154.
[2] M.P. Bondar, V.F. Nesterenko, J. Phys. IV (Colloque C3) 1 (1991) 163.
[3] V.F. Nesterenko, M.P. Bondar, Dymat J. 1 (1994) 245.
[4] S. Nemat-Nasser, M. Hori, J. Appl. Phys. 62 (1987) 2746.
[5] S. Nemat-Nasser, S.-N. Chang, Mech. Mater. 10 (1990) 1.
[6] A.M. Cuitino, M. Ortiz, Acta Mater. 44 (1996) 427.
[7] S. Nemat-Nasser, T. Okinaka, Mech. Mater. 24 (1996) 43.
[8] R. Hill, J. Mech. Phys. Solids. 14 (1966) 95.
[9] J.R. Rice, J. Appl. Mech. 37 (1970) 728.
[10] R. Hill, J.R. Rice, J. Mech. Phys. Solids. 20 (1972) 401.
[11] S. Nemat-Nasser, J. Appl. Mech. 50 (1983) 1114.
[12] R.J. Asaro, J. Appl. Mech. 50 (1983) 921.
[13] K.S. Havner, Finite Plastic Deformation Of Crystalline Solids, Cambridge University Press, Cambridge, NY, 1992.
[14] S. Nemat-Nasser, Y.-F. Li, J.B. Isaacs, Proc. MEET'N'93, the 1st Joint Meet ASCE, ASME, and SES, Experimental Techniques in the Dynamics of Deformable Solids, Charlottesville, VA, 1993 p. 25.
[15] M.M. Rashid, S. Nemat-Nasser, Comp. Method Appl. Mech. Eng. 94 (1992) 201.